Tailored Electron Transfer Pathways in Aucore /Ptshell -Graphene Nanocatalysts for Fuel Cells

Seselj, Nedjeljko; Engelbrekt, Christian; Ding, Yi; Hjuler, Hans Aage; Ulstrup, Jens; Zhang, Jingdong

Published in:
Advanced Energy Materials

Link to article, DOI:
10.1002/aenm.201702609

Publication date:
2018

Document Version
Peer reviewed version

DOI: 10.1002/ ((please add manuscript number))
Article type: Full Paper

Tailored electron transfer pathways in Au_{core}/Pt_{shell}–graphene nanocatalysts for fuel cells

*Nedjeljko Seselj, Christian Engelbrekt, Yi Ding, Hans A. Hjuler, Jens Ulstrup, Jingdong Zhang**

Mr. N. Seselj, Dr. C. Engelbrekt, Prof. J. Ulstrup, Prof. J. Zhang
Department of Chemistry, Technical University of Denmark (DTU), Kemitorvet, Building 207, 2800 Kgs. Lyngby, Denmark
E-mail: jz@kemi.dtu.dk
Prof. Y. Ding
Institute for New Energy Materials and Low-Carbon Technologies, Tianjin University of Technology, Tianjin, 300384, P.R. China
Dr. H. A. Hjuler
Danish Power Systems Ltd, Egeskovvej 6C, DK-3490 Kvistgård, Denmark

Keywords: graphene, Au-Pt core-shell, fuel cells, electron pathway

Au_{core}/Pt_{shell}-graphene catalysts (G-Cys-Au@Pt) have been prepared through chemical and surface reactions. Au-Pt core-shell nanoparticles (Au@Pt NPs) covalently immobilized on graphene (G) are utilized as efficient electrocatalysts in low-temperature polymer electrolyte membrane fuel cells (FCs). The 9.5 ± 2 nm Au@Pt NPs with atomically thin Pt shells are attached on graphene via L-cysteine (Cys), which serve as linkers controlling the NP loading and dispersion, enhancing the Au@Pt NPs stability, and facilitating interfacial electrochemical electron transfer. The increased activity of G-Cys-Au@Pt, compared to non-chemically immobilized G-Au@Pt and commercial platinum NPs adsorbed on graphitized carbon (C-Pt), is a result of (1) the tailored electron transfer pathways of covalent bonds integrating Au@Pt NPs into the graphene framework, and (2) synergetic electronic effects of atomically thin Pt shells on Au cores.
Enhanced electrocatalytic oxidation of formic acid (FA), methanol (MeOH) and ethanol (EtOH) is observed as higher specific currents and increased stability of G-Cys-Au@Pt compared to G-Au@Pt and C-Pt. Dioxygen reduction on G-Cys-Au@Pt occurs at 25 mV lower potential and 43 A g_{Pt}^{-1} (at 0.9 V vs. RHE) higher current than for C-Pt. Functional tests in direct FA, MeOH and EtOH FCs exhibit 95, 53 and 107 % increased power densities for G-Cys-Au@Pt over C-Pt, respectively.

1. Introduction

As clean and sustainable energy technology, fuel cells (FCs) generate electricity using chemical energy stored in fuel molecules. Catalysts are crucial in the performance and cost of FC systems. As the most efficient catalyst for FCs, platinum (Pt) has been widely used for both anodes and cathodes in polymer electrolyte membrane fuel cells (PEMFCs). However, the high price of Pt, poisoning by CO-like intermediates and challenges regarding stability drive us to develop catalyst systems ultra-low in Pt, Pt-free transition metals and even using enzymes or biological

cells.[1][2][3] Increasing the electrochemically active surface area (ECSA) of Pt-based catalysts by nanostructure formation offers an approach to optimize their catalytic activity. Reducing the nanoparticle (NP) size decreases the relative amount of Pt needed and boosts the specific ECSA, resulting in better catalytic performance. However, a size limitation occurs around 2.2 nm, below which the activity declines due to the loss of low-index crystal faceting and aggregation during the catalysis.[4] Nanostructured material properties significantly depend on chemical composition, size, crystallinity and morphology. Bimetallic core-shell NPs reduce the amount of inactive bulk atoms, at the same time preserving the crystalline surface faceting of the target Pt shell. Synergetic effects between core and shell can even reduce catalytic poisoning.[5]
Replacement of inactive Pt bulk by gold (Au) produces stable NPs with more efficient Pt utilization.[6] Au nanostructures have been widely studied and their application as CO oxidation catalysts are well established.[7] Moreover, having an atomic diameter close to Pt and being a stabilizing agent for reactions in PEMFC application,[6][8] Au is an ideal candidate for core material in core-Pt_{shell} NP architectures. We have developed Au-Pt core-shell NPs (Au@Pt NPs) using a green glucose- and starch-based recipe.[9] The Au@Pt NPs show good catalytic activity towards electrochemical oxidation of sustainable fuels such as formic acid, methanol and ethanol, as well as selective hydrogenation of benzene derivatives.[9] The present Au can easily oxidize catalytic poisons generated from small organic molecules oxidizing on Pt.[10] We therefore wish to pursue further development of electrocatalysts based on Au@Pt NPs for FC systems. The new Au@Pt NPs may therefore hold a perspective for large-scale production of catalysts that requires uniform products prepared under mild conditions with low cost.
A suitable support material with strong interactions with the target NPs is, however, needed to fully exploit the catalyst function. Stability and conductivity of the catalysts are essential, i.e. fast electron transfer from the active site at the catalyst surface through the support material to the external circuit. Carbon black or graphitized carbon black are commercially used as support materials for Pt NPs in PEMFC application.[11] However, these carbon materials can be oxidized at potentials above 0.8 V vs. standard hydrogen electrode (SHE). The resulting conductivity degradation leads to loss of FC performance.[12] Such issues can be effectively avoided by the use of graphene as a supporting material, due to its large surface area (2600 m^2g^{-1}), chemical inertness under PEMFC operating conditions and high electrical conductivity.[13] Graphene has been used as a support for metal NPs such as Pt[14], Pt-Fe[15], Pt-Co[15], Pt-Au alloy[16], and Fe/Co-N[17]. In the present work, we demonstrate a three-step method for the preparation of electrocatalysts equipped with 9.5 ± 2 nm Au@Pt NPs covalently anchored on graphene (G-Cys-Au@Pt). The Au@Pt NPs with atomically thin Pt shells are synthesized using 2-(N-morpholino)ethanesulfonic acid (MES) and glucose as environmentally harmless reducing and shape-directing agents. High loading of uniformly distributed Au@Pt NPs on graphene was achieved through covalent bonding via L-Cysteine (Cys) molecules. Graphene precursor, graphene oxide (GO), was functionalized by Cys via 1-Ethyl-3-(3-dimethylaminopropyl)carbodiimide (EDC) and N-Hydroxysuccinimide (NHS) surface-based coupling reactions, while Au@Pt NPs were immobilized on Cys anchors by covalent thiol-Au bonds. Cys linked G-Cys-Au@Pt electrocatalyst exhibited high activity for FA, MeOH and EtOH electrochemical oxidation, as well as for oxygen reduction reaction (ORR). The G-Cys-Au@Pt catalyst was further applied in direct formic acid fuel cell (DFAFC), direct methanol fuel cell (DMFC) and direct ethanol fuel cell (DEFC) for functional tests. Pt-based commercial catalyst was utilized as a reference in power density and stability analysis, and superior performance was found for the G-Cys-Au@Pt catalyst. Systematic structure and compositional mapping suggests that the enhanced performance originates from (1) the tailored electron transfer pathway through the Cys linker of G-Cys-Au@Pt, (2) improved Pt utilization and activity from synergy between atomic Pt shell and Au core, (3) covalent and stable anchoring of catalyst NPs, and (4) the highly conductive and robust graphene support.

2. Results and Discussion

2.1 Chemical syntheses of cysteine-linked Au@Pt NPs on graphene

The syntheses of G-Cys-Au@Pt catalysts are briefly described in Scheme 1. GO was prepared by a modified Hummer's method,[18] where single-layered sheets of thickness 0.9 nm and lateral dimensions ranging from several hundred nanometers to 5 µm were obtained and verified by atomic force microscopy (AFM), Figure S1. The G-Cys-Au@Pt nanocatalyst was prepared by a green, three-step synthesis route consisting of (1) GO functionalization with Cys followed by formation of (2) Au NPs as cores and (3) Au core-Pt shell NP preparation. The Cys linker was introduced to the GO in the presence of EDC and NHS coupling reactions in aqueous environment followed by hydrothermal reduction, resulting in G-Cys in which the amine group of Cys is covalently anchored on graphene. The thiol group was utilized to attract gold atoms for immobilization of Au NP cores on the graphene (G-Cys-Au). Pt precursor was subsequently slowly added and reduced by glucose, forming atomically thin Pt shells around the anchored Au NP cores (G-Cys-Au@Pt). The color of the colloidal suspension changed from black of G-Cys to dark-red of G-Cys-Au and dark-brown of the final product, G-Cys-Au@Pt (Figure S2). The synthesized G-Cys-Au@Pt nanocatalyst was purified and concentrated by repeated centrifugation and redispersion in ultrapure water. As a reference, Pt NPs were synthesized through the same route and immobilized on G-Cys. These are noted as G-Cys-Pt, Figure S3. G-Cys-Pt showed a morphological difference from G-Cys-Au@Pt with a narrow and homogeneous Pt NPs size distribution of 1.2 ± 0.8 nm. The controllable loading of Au@Pt NPs on graphene was achieved by tuning the density of Cys on GO. The regulating parameter crucial for quantitative coupling of Cys to graphene was altering the concentrations of EDC (from 2.5 to 5.0 mM) and NHS (from 2.0 to 5.0 mM) used in the G-Cys synthesis route. It allowed for high or low surface coverage of graphene adsorption sites available for Cys to attach, depending on higher or lower EDC and NHS concentrations used, respectively.

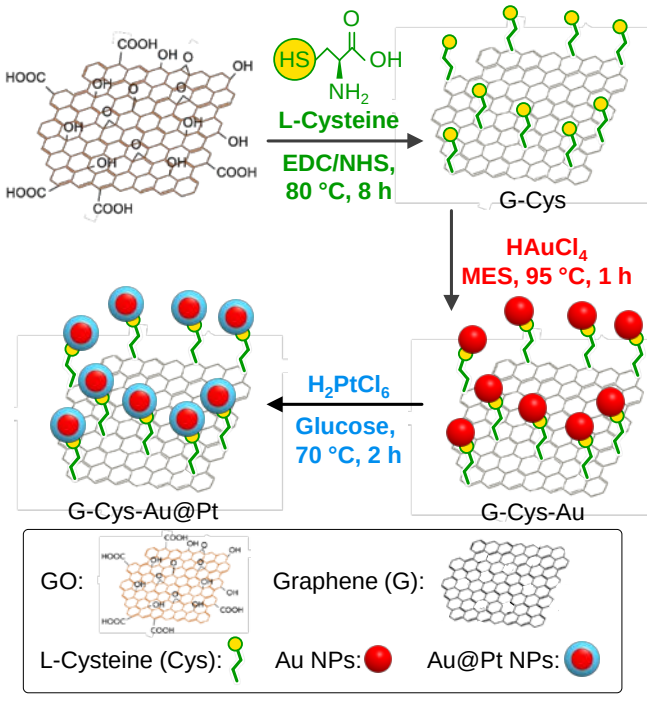

Scheme 1. Three-step synthesis route of G-Cys-Au@Pt: 1) GO functionalization with Cys via EDC/NHS coupling and thermal reduction to graphene, G-Cys, 2) Au NPs synthesis and anchoring through Au-S bonding, G-Cys-Au, 3) Pt shell growth on the Au NPs by reduction of $PtCl_6^{2-}$ to form G-Cys-Au@Pt.

2.2 Structure, compositions and optical properties

The morphology, size and elemental composition of the synthesized materials were mapped by transmission electron microscopy (TEM), high-resolution TEM (HR-TEM), Figure 1, and by energy-dispersive X-ray spectroscopy (EDX), Figure S4. G-Cys is composed of Cys-modified graphene sheets ranging from hundreds of nanometers to 5 µm, confirmed by TEM, Figure 1A and XPS, Figure S8B. Au NP synthesis conducted in the presence of G-Cys resulted in uniform NPs of 9.5 ± 1.8 nm, immobilized on the graphene (G-Cys-Au), Figure 1B. Subsequent chemical deposition of Pt shells on the Au-cores generated G-Cys-Au@Pt, Fig. 1C-D. EDX measurements confirm that the G-Cys-Au@Pt particles contain 75 ± 1 % Au and 25 ± 1 % Pt. The metal ratio in G-Cys-Au@Pt was supported by inductively coupled plasma optical emission spectrometry (ICP-OES) giving 74 ± 1 % Au and 26 ± 1 % Pt, Figure S5. The catalyst metal loading was determined by thermogravimetric analysis (TGA) to be 42 wt. %, Figure S6. The size of the Au@Pt NPs from TEM was found to be 9.5 ± 2 nm (Figure 1C), was in fact almost identical to the size of the Au NP in G-Cys-Au. The atomically thin Pt shells (3-4 Å) on Au NPs were hardly detectable directly from TEM (Figure 1D) and instead evaluated on the basis of the metal ratio and NP size obtained from EDX (Figure S4) and TEM, as established previously.[6] Scanning TEM (STEM) equipped with EDX elemental mapping was used to investigate Au and Pt distributions in G-Cys-Au@Pt, Figure 1E-H and Figure S7. High resolution elemental mapping of Au@Pt NPs indicates that Pt signals come from the entire area of NPs, however mostly from the NP perimeter (Figure 1H) corroborating the core-shell structure. An overview of the spectroscopic characterization of component interactions in the G-Cys-Au@Pt catalysts is shown in Figure 2.

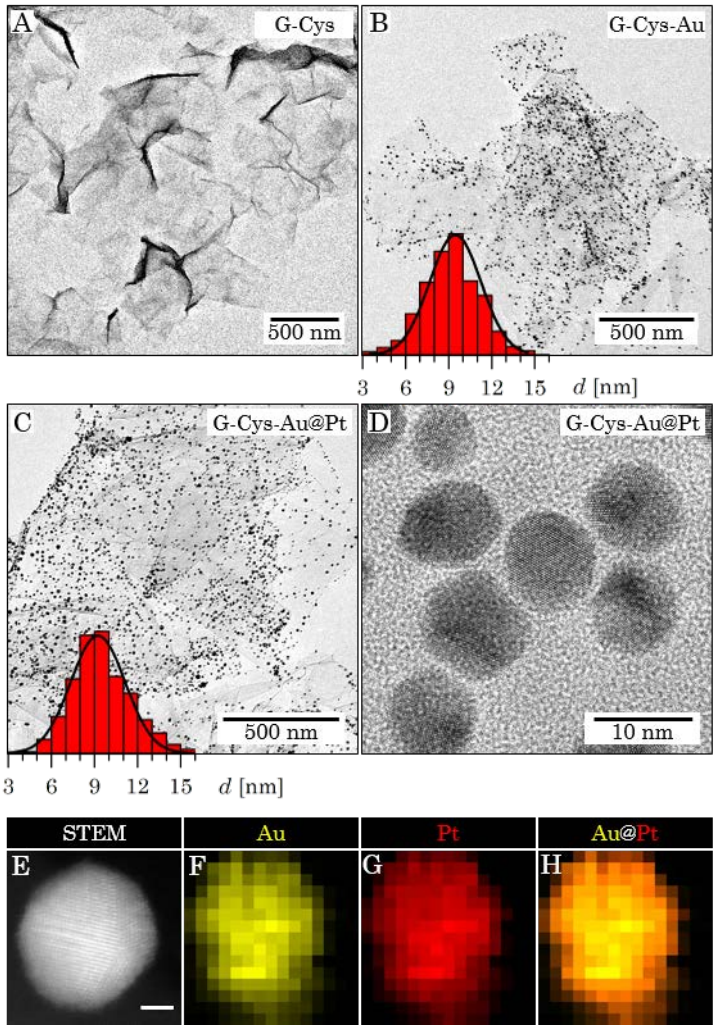

Figure 1. TEM images of (A) G-Cys, (B) G-Cys-Au and (C) G-Cys-Au@Pt. The size distributions of Au@Pt NPs are shown as inset in (B) and (C). (D) HR-TEM image of G-Cys-Au@Pt. (E) STEM image of Au@Pt NP with EDX elemental mapping of (F) Au, (G) Pt, and (H) composition image of both Au and Pt signals. Scale bar in E is 2 nm.

The evidence of Pt shells around Au NPs is supported by the UV-vis spectra. Damping and broadening of the Au NP localized surface plasmon resonance (LSPR) peak at 520 nm strongly indicates Pt shell formation, Figure 2A. Such observations agree with reports for a variety of core-Pt_{shell} NPs.[19] The UV-vis spectra of the synthesized G-Cys-Au@Pt catalyst and its constituents are presented in Figure 2B. Two GO-characteristic absorption peaks at 232 and 301 nm, from $\pi \rightarrow \pi^*$ transitions in aromatic C=C bonds, and $n \rightarrow \pi^*$ transitions in C=O bonds, respectively[20] are observed. Upon GO reduction, graphene exhibits a single characteristic peak at 269 nm due to the restoration of the original electronic conjugation. The presence of the Pt shell around the Au NP core surface results in red-shift and damping of the LSPR peak. G-Cys-Au@Pt, i.e. Au@Pt NPs immobilized on graphene cause further red-shift and broadening of the LSPR peak, Figure 2B, due to altering the localized electromagnetic field.[21] The electric field distortion is greatly amplified by chemical bonds between the Au@Pt NPs and graphene acting as a direct electron sink. Fast electron transfer is essential for high catalytic rates. Ideally, a short chain length of the linker molecule between the catalytically active sites and the electrode enhances the electron transfer rate.[22]

As a short organic molecule with only three carbon atoms, Cys is specifically chosen as a linker due to the ability of selectively bonding to graphene and Au NPs via amine and thiol groups,

respectively. The interconnected structure of G-Cys-Au@Pt and the presence of Cys covalent bonding was studied by X-ray photoelectron spectroscopy (XPS), Figure 2D-F. XPS spectra of S 2p, deconvoluted into spin-orbit doublets at 162.2 and 163.1 eV are assigned to S–Au interactions.[23] This shows that covalent thiol-Au bonds have successfully integrated Au@Pt NPs into the graphene framework. Peaks at 163.8 and 165.0 eV are from free thiol (-SH)[23][24] and peaks at 166.9 and 168.2 eV from SO_3^- [25] in the MES capping around the NP surface. The SO_3^- species dominate the sulfur spectrum due to a larger NP surface coverage than the local thiol-NP bonding sites of Cys. This is confirmed in the S XPS spectrum of G-Cys (Figure S8B) and pure Au@Pt NPs (Figure S8C). The S spectrum of G-Cys showed no S–Au (162.2 eV) and SO_3^- (166.9 eV) peaks, while SO_3^- peaks dominate the Au@Pt S spectrum. Peaks at 169.2 and 170.4 eV represent a small amount of oxidized sulfur in the form of SO_4^{2-} species.[26] Similarly, the C 1s spectrum (Figure 2F) is deconvoluted into peaks at 284.6, 286.0, 287.4 and 288.6 eV, assigned to C–C, C–O, C=O and COO^-, respectively.[27] Small peaks at 285.9 eV and 287.1 eV have been found in N-doped graphene for N–C(sp^2) and N–C(sp^3) bonds, respectively.[28] These features are difficult to distinguish in the G-Cys C spectrum (Figure S8B). Therefore, the presence of N–graphene bonds is evidenced in the N 1s XPS spectrum of G-Cys-Au@Pt (Figure 2E). Three peaks are centered at 398.2 eV, 400.0 eV and 402.1 eV, corresponding to metal-nitrogen (Me-N) bond,[29] amide, and oxidized N (N_{ox}), respectively.[28] The Me-N peak originates from MES at the Au NP surface, dominating the N spectrum due to significantly larger domains of MES capping than Cys anchors. This is in contrast to the N spectrum of G-Cys (Figure S8B) which does not contain the Me-N peak. On the other hand, the N spectrum of pure Au@Pt NPs (Figure S8C) is dominated by Me-N peak, proving that MES is binding to Au@Pt NPs through N bonding. Amide N signals come from chemical bonds between graphene and Cys.[30] There is a weak N_{ox} peak caused by oxidized N species (Figure 2E), also present in the N spectrum of G-Cys (Figure S8B). Both C and N XPS spectra clearly confirm that graphene has become functionalized with Cys dominated by amide chemical bonds, and covalent attachment of Au@Pt NPs to graphene through the Cys linker. An electron pathway between the graphene and Au@Pt NPs via the Cys linker in G-Cys-Au@Pt has thus been created.

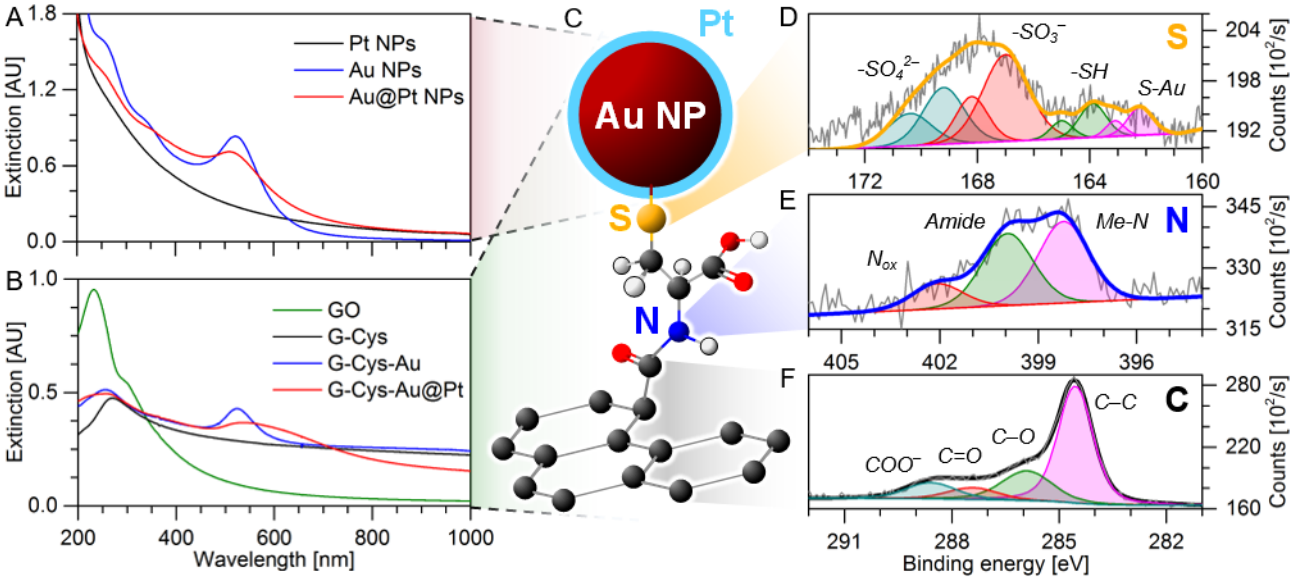

Figure 2. UV-vis spectra analysis of (A) unsupported Pt (black), Au NPs (blue) and Au@Pt (red) NPs; (B) purified GO (green), G-Cys (black), G-Cys-Au (blue) and G-Cys-Au@Pt (red). (C) Schematic representation of G-Cys-Au@Pt. G-Cys-Au@Pt elemental XPS analysis of: (D) sulfur, (E) nitrogen and (F) carbon spectra.

2.3 Electrochemical properties and electrocatalysis

2.3.1 Stability of G-Cys-Au@Pt in oxidative voltammetric cycles

Electrochemical oxidation of L-Cys oxidation on metal electrodes has been reported comprehensively.[31][32][33] The dimer, L-cystine central intermediate[31] at both platinum and gold electrodes in the potential range 0.8-1.2 V, as described by the following:[34]

$$RSH \leftrightarrow RSH_{(ads)} \quad (1)$$
$$2RSH_{(ads)} \rightarrow 2RS^{\bullet}_{(ads)} + 2H^{+} + 2e^{-} \quad (2)$$
$$2RS^{\bullet}_{(ads)} \leftrightarrow RSSR \quad (3)$$

The formed L-cystine is further oxidized at 1.0 V via reactions:

$$RSSR \leftrightarrow 2RS^{\bullet}_{(ads)} \quad (4)$$
$$2RS^{\bullet}_{(ads)} + 3H_2O \rightarrow RSO_3^{-} + 6H^{+} + 5e^{-} \quad (5)$$
$$2RS^{\bullet}_{(ads)} + 2H_2O \rightarrow RSO_2^{\bullet} + 4H^{+} + 4e^{-} \quad (6)$$

These processes could apply also to the L-Cys linker with risk of degradation of the central catalytic G-Cys-Au@Pt unit. We therefore investigated separately the anodic voltammetry of solute L-Cys on both G-Cys-Au@Pt and G-Au@Pt electrode surfaces. Similar investigations for 2-aminoethanethiol (no carboxylate group), propionic acid (only the carboxylate functional group), and L-alanin (no functional groups) were also undertaken,

Details of this investigation are given in the Supporting Information and Figures S9-S14. The conclusion is that the G-Cys-Au@Pt unit retains full functional integrity in the oxidation processes of bulk L-Cys. This important observation also raises the question why the G-Cys-Au@Pt unit retains its integrity under conditions where bulk solute L-Cys is oxidized. It can here be argued, first that L-Cys linker is bound in rigid surface binding configurations via randomly distributed, spatially separated G-surface functionalities. Lerf and associates thus investigated the structure of GO by ^{13}C and ^{1}H nuclear magnetic resonance spectroscopy (NMR).[35] They showed that (1) the distribution of functional groups in oxidized aromatic rings are not identical and are distributed randomly, and (2) carboxylic acid groups are present in rather low quantities (compared to keto groups) positioned mostly at defect sites and the periphery of nanosheets.[36][37] It is therefore, reasonable to conclude that 9.5 nm Au@Pt NPs attach to multiple, immobile Cys linkers enough separated from each other to prevent surface mobility of $RS^{\bullet}_{(ads)}$ and formation of S–S bonds during oxidation. It is therefore understandable that L-Cys in the special dual-linked configuration can behave quite differently compared with L-Cys in solution.

2.3.2 Oxidative desorption of adsorbed carbon monoxide and hydrogen

It was discovered recently that Pt–Au NPs offer efficient catalysis towards oxidation of small organic molecules with less adsorbed CO (CO_{ads}) than on pure Pt surfaces,[10] suggesting a potential application of Au@Pt NPs in FCs. The electronic properties of the new G-Cys-Au@Pt were investigated by electrochemical techniques. Three new main features are observed compared to platinum nanoparticles ($\leq$ 5 nm) on graphitized carbon catalyst (C-Pt): (1) The Pt-specific hydrogen region has been augmented from 264 mV for C-Pt to 317 mV for G-Cys-Au@Pt, (2) the Pt_{oxide} reduction peak experienced a 37 mV positive shift for G-Cys-Au@Pt while (3) the Au_{oxide} reduction peak was shifted 35 mV negatively compared to a single-crystal Au(111) surface, Figure S15. Such electronic modifications of Pt in the shell benefit the

interactions with the target fuel molecules by increasing the adsorption energy.[38] Possible catalytic oxidation of the Cys linkers was investigated and found to not take place under the conditions used for the electrochemical studies. A detailed discussion is given in the supporting information.

Cyclic voltammetry was used to study CO oxidative desorption on G-Cys-Au@Pt and C-Pt catalysts, Figure 3. Both catalysts were conditioned at -0.2 V during CO adsorption from CO-saturated 0.10 M H_2SO_4. Solid lines in the plots represent the first cycles in which CO is desorbed from the catalyst surfaces during the anodic scans, and dashed lines the second cycles with full catalyst profile restoration. At scan rate of 50 mV s^{-1} CO oxidation on C-Pt starts at 0.420 V and exhibits a sharp peak with the maximum at 0.521 V, while the onset on G-Cys-Au@Pt NP is shifted positively to 0.440 V and the maximum to 0.527 V. This positive potential shift for G-Cys-Au@Pt is usually recognized as hindered CO oxidation due to stronger adsorption on Au-modified Pt surface.[39] Heterometallic bonding induces tensile strain on the Pt shells because of a different lattice constants from Au. Effectively, the Pt d-band energy is increased resulting in stronger bonding to CO.[40] However, Au acts as an excellent catalyst for CO oxidation[41] and when introduced to Pt, the number of active sites available for CO adsorption decreases. The resulting effect is a decrease in Pt poisoning for G-Cys-Au@Pt. Integrating the peaks provides the charges associated with CO (A_{CO}) and hydrogen ($A_{H\text{-}UPD}$) desorption, where $A_{H\text{-}UPD}$ represents the total electrochemically active Pt surface area (ECSA). The ratio between the two gives the index of CO poisoning per Pt surface area ($CO/ECSA_{Pt}$). G-Cys-Au@Pt $A_{H\text{-}UPD}$ and A_{CO} were 104.76 and 115.87 $m^2\ g_{Pt}^{-1}$, respectively. C-Pt $A_{H\text{-}UPD}$ is 41.27 and A_{CO} 52.38 $m^2\ g_{Pt}^{-1}$. Figure 3A and B show $CO/ECSA_{Pt}$ indexes of 1.11 (G-Cys-Au@Pt) and 1.27 (C-Pt), i.e. 14 % more CO is adsorbed on C-Pt than on G-Cys-Au@Pt. Insets in Figure 3 show the CO desorption peaks at a slow scan rate, i.e. 10 mV s^{-1}. G-Cys-Au@Pt undergoes a significant peak shift towards negative values, stabilizing at 0.487 V, while C-Pt has an oxidation peak at 0.555 V. The more efficient CO_{ads} removal on G-Cys-Au@Pt at low scan rates is contrary to the postponed CO_{ads} oxidation at fast scan rates. At slow scan rate the d-band effect is no longer dominating the CO_{ads} oxidation, as evidenced from the negative shift of the reaction potential. This can be explained by (1) diffusion issues through graphene layers and (2) low mobility of CO due to the low potential at which the adsorption and oxidation processes take place. If zero mobility of CO molecules is assumed, only CO adsorbed at the Pt step sites would be oxidized.[42] In case the diffusion rate is slow, CO molecules close to the Pt step sites can also get oxidized (along with the already step-adsorbed CO molecules) during the time in which the CO_{des} peak appears.[42] Depending on the time window of the experiment (scan rate) the peak potential and charge can therefore, be changed. At higher scan rates (50 mV s^{-1}) there is not enough time for CO molecules to adsorb/desorb to/from the Pt shell. This results in 6 mV larger overpotential on G-Cys-Au@Pt than on C-Pt. Additionally, layered graphene structure extends the pathway for CO to diffuse in or out of G-Cys-Au@Pt which further promotes the phenomenon. On the other hand, at steady-state conditions, the diffusion effect is not as pronounced and the CO oxidation on G-Cys-Au@Pt occurs at 68 mV lower overpotential. The enhancement of the catalytic properties will be further demonstrated in studying dioxygen reduction and oxidation of fuel molecules, Sections 2.3.3 and 2.3.4, representing the reactions at FC cathode and anode, respectively.

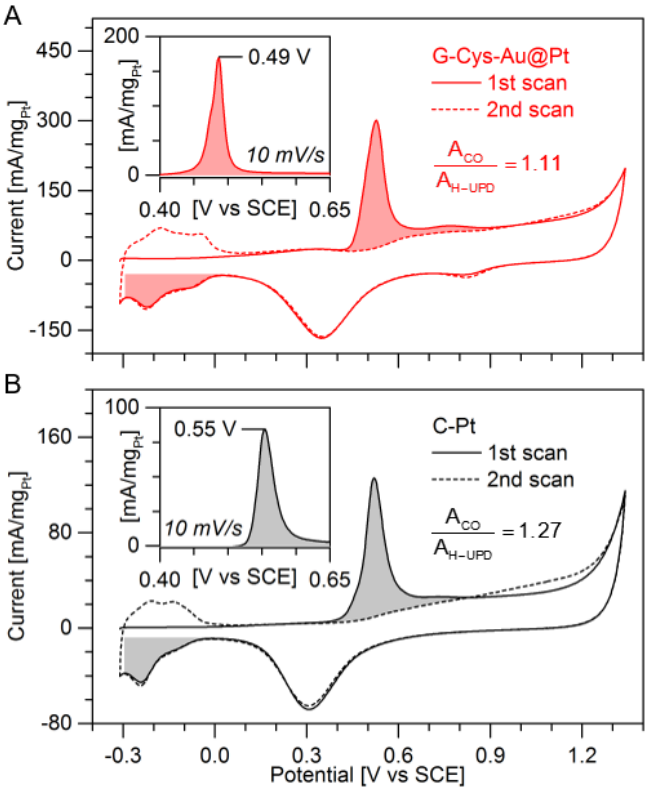

Figure 3. CO desorption from CO-saturated Pt surfaces (solid line), and clean, CO-free surfaces (dashed line), for (A) G-Cys-Au@Pt and (B) C-Pt catalysts. The charges associated with CO and hydrogen desorption at ca. 0.5 and -0.2 V, respectively, are indicated with filled areas. Cyclic voltammograms in 0.10 M H_2SO_4 were recorded at 50 mV s^{-1} while insets represent CO oxidation at 10 mV s^{-1}.

2.3.3 The electrochemical dioxygen reduction reaction (ORR)

The electrocatalytic activity for oxygen reduction reaction (ORR) was examined by voltammetry in oxygen-saturated 0.10 M $HClO_4$ solution. Figure 4A and B show the catalytic responses of G-Cys-Au@Pt and C-Pt, respectively, in Ar- (dashed lines) and oxygen-saturated (solid lines) electrolyte. Both catalysts electrocatalyse ORR, as observed from the cathodic peak at ~ 0.410 V, with the onsets at 0.540 V for G-Cys-Au@Pt and 0.498 V for C-Pt, indicating slightly lower overpotential towards ORR on G-Cys-Au@Pt. However, a larger current density change between Ar and O_2 saturated solution is found on C-Pt, implying better catalytic performance than on G-Cys-Au@Pt. This is caused by diffusion limitations of the graphene-based catalysts. The packing of graphene sheets during G-Cys-Au@Pt deposition and drying on the electrode extends the pathway of dioxygen molecules through the graphene layer compared to carbon black particles.[43] Even small molecules can be trapped within the graphene sheets effectively hindering a reaction in which the reactant diffuses to the catalyst surface. Diffusion of dioxygen through the graphene layers therefore plays a role in the catalyst efficiency. This was supported by rotating disk and ring-disk electrode techniques, in which diffusion and kinetics at the electrode surface are separated. Figure 4C and S16A-B show rotating ring-disk electrode (RRDE) cathodic linear sweep voltammograms of C-Pt (black) and G-Cys-Au@Pt (red) at 1600 rpm. Solid and dashed lines represent currents from dioxygen reduction (at the disk electrode) and the corresponding H_2O_2 oxidation (at the ring electrode), respectively. The C-Pt catalyst exhibits an onset potential at 950 mV, and a half-wave potential (E_{HW}) of 870 mV vs. RHE, consistent with previous reports[44]. The onset potential and E_{HW} are shifted to 1.00 V and 895 mV vs. RHE, respectively, for the G-Cys-Au@Pt catalyst. This 25

mV overpotential reduction for ORR on the G-Cys-Au@Pt results in a catalytic activity of 132 A g_{Pt}^{-1} (at 0.900 V) outperforming C-Pt by 43 A g_{Pt}^{-1}, an increase of around 50 %. G-Au@Pt catalyst was tested towards ORR as well, Figure S16C. Limiting currents were significantly lower than for G-Cys-Au@Pt with the reaction overpotential of 364 mV on G-Au@Pt. Lower currents indicate inaccessibility or poor Pt contact to the electrode. The absence of Cys linkers in G-Au@Pt inhibited the electrocatalysis due to the insufficient integration of Au@Pt NPs on graphene nanosheets. This acts as a limiting feature in the G-Au@Pt structure.

Dioxygen reduction proceeds either via a direct 4-electron pathway or via an unfavorable 2-electron formation of peroxide.[45] The electron-transfer mechanism of ORR was not quantified by the Koutecky-Levich analysis since recent studies have pointed out the unreliability of this method due to the relative errors of kinetic current density, standard rate constant and the calculation errors originating in disregarding the kinetic terms of the equation.[46] Instead, the electron transfer number (n) was estimated from the ratio of the experimentally obtained currents at the disk (I_D) and the ring (I_R) electrodes:[47]

$$n = \frac{4I_D}{I_D + \left(\frac{I_R}{N}\right)} \quad (1)$$

where N is the current collection efficiency coefficient. The inset in Figure 4C highlights that both catalysts reduce dioxygen to water almost exclusively through the direct 4-electron pathway, $O_2 + 4H^+ + 4e^- \rightarrow 2H_2O$, but it is noted that G-Cys-Au@Pt demonstrates a higher reaction efficiency in the entire potential range. The synergetic interaction between Au core and Pt shell thus enhances kinetically the catalytic performance for ORR, evidenced by more positive half-wave and onset potentials, as well as higher electron transfer numbers than for C-Pt. Such enhanced catalysis for the system core reaction holds promise for appropriate application of G-Cys-Au@Pt as a cathode catalyst in FCs.

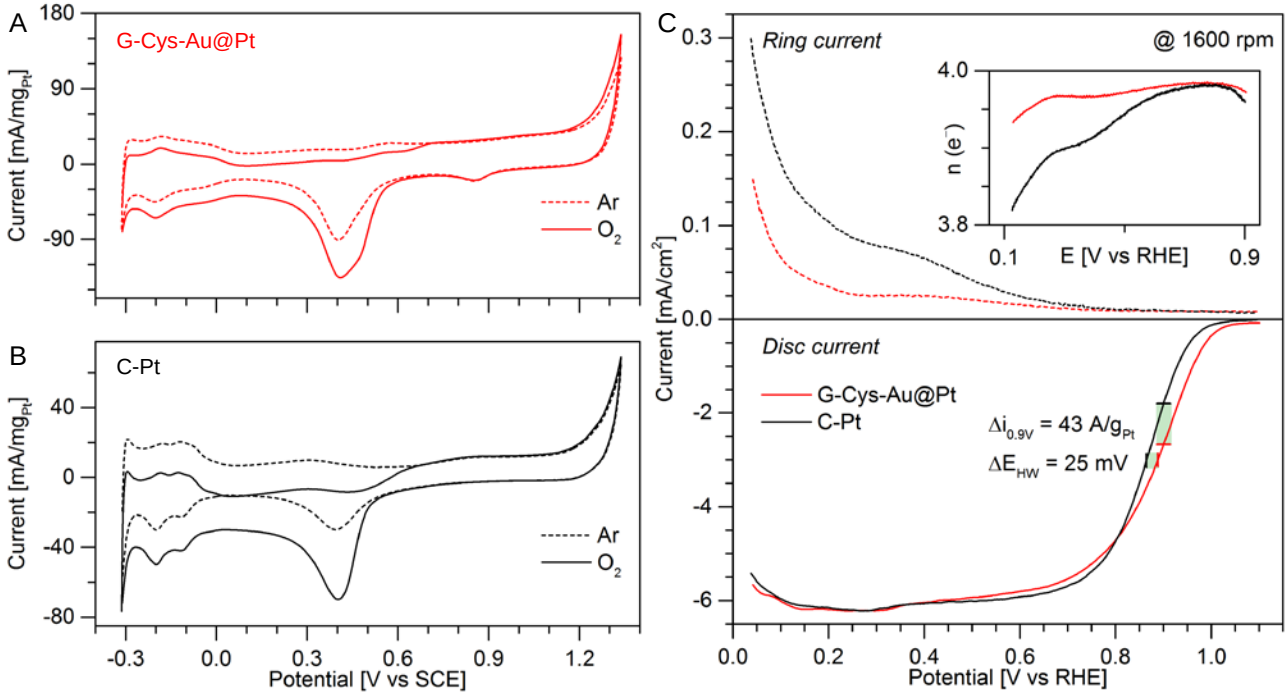

Figure 4. Cyclic voltammetry of (A) G-Cys-Au@Pt and (B) C-Pt in oxygen saturated 0.10 M $HClO_4$ (solid lines) and Ar (dashed lines) at 50 mVs^{-1}. (C) Voltammetry of RRDE on the ring electrode (upper) and disk electrode (bottom) for G-Cys-Au@Pt (red) and C-Pt (black). Disk currents represent catalyst performance towards ORR (solid lines) and ring currents simultaneous oxidation of H_2O_2 formed during ORR (dashed lines). Linear sweep voltammetry

at 20 mV s^{-1} and 1600 rpm in dioxygen saturated 0.10 M $HClO_4$. The Pt ring potential was kept at 1.1 V vs. RHE. Pt loading of G-Cys-Au@Pt and C-Pt catalysts was 20.2 $\mu g_{Pt}\,cm^{-2}$.

2.3.4 Oxidation of fuel cell target molecules

The catalytic performance of G-Cys-Au@Pt was further explored by conducting electrochemical oxidation of 0.10 M target fuel molecules in 0.10 M H_2SO_4 supporting electrolyte, i.e. formic acid (FAOR), methanol (MOR) and ethanol (EOR) oxidation reactions, Figure 5. FAOR voltammetry displays four typical peaks, three in the anodic and one in the cathodic scan, Figure 5A. Peak (1) at ca. 0.3 V originates from oxidation of adsorbed formate to CO_2 (the direct pathway) which is then suppressed by the subsequent adsorption of CO.[48] The 0.6 – 0.7 V anodic and sharp peak represents the oxidation of CO_{ads} to CO_2 (the indirect path), while the 1.2 V anodic and broad peak appears is caused by the reaction of intermediates and FA at the oxidized Pt surface.[48] The very strong and sharp cathodic scan peak at ~ 0.3 V originates from the direct oxidation of HCOOH to CO_2 at the freshly reformed Pt surface following reduction of Pt_{oxide}.[49] 4.4 times higher currents (464 mA mg_{Pt}^{-1}) were obtained for the G-Cys-Au@Pt at 0.3 V, than for C-Pt. Compared with recently reported, state-of-the art catalysts, the G-Cys-Au@Pt exhibits comparable performance even with 5 times lower fuel molecule concentration.[50][51][10] Figure 5B shows the chronoamperometric response on both G-Cys-Au@Pt and C-Pt catalysts for FAOR. The oxidizing potential (E_{ox}) was kept at 0.10 V and currents monitored for 6000 s. The final current values and the decay slope indicates higher catalyst stability for G-Cys-Au@Pt with 2.3 times higher currents than C-Pt at the end of the measurements.

Similarly, MOR in Figure 5C produces four peaks. These peaks originate from close-lying direct/indirect MeOH oxidation at 0.5 V. [48] G-Cys-Au@Pt shows 674 mA mg_{Pt}^{-1} for the anodic peak at ca. 0.6 V representing the indirect MeOH oxidation via CO adsorbate - 3.2 times higher than the corresponding C-Pt peak. Even for 5 to 10 times lower MeOH concentrations employed here, the electrocatalytic performance of G-Cys-Au@Pt exceeds, or is similar to recently reported electrocatalysts.[52][53] Figure 5D shows the stability of catalytic currents at 0.3 V over 6000 s, with the current density for G-Cys-Au@Pt 6.4 times that of C-Pt at the end of the measurements.

EOR profiles of G-Cys-Au@Pt and C-Pt catalysts are presented in Figure 5E. Due to the need for C–C bond breaking for full oxidation of EtOH, EOR often gives low current densities. The anodic peak at 0.7 V represents the reaction pathway via CO_{ads} oxidation where G-Cys-Au@Pt exhibits 406 mA mg_{Pt}^{-1}, and 3.8 times larger currents than those obtained with C-Pt and greatly improved stability with currents 4.4 times higher after 6000 s of continuous reaction, Figure 5E-F. A plethora of catalysts has been studied for EOR in both acidic and alkaline environments. Akhairi et al. reported the significance of fuel concentration on the FC performance, showing 4 times higher current densities for EOR in 1.0 M compared to 0.10 M ethanol with a Pt/C catalyst.[54] Our experiments show that G-Cys-Au@Pt gives enhanced catalytic behavior compared to recently reported Pt catalysts, tested in acidic conditions and with 10 times higher EtOH concentration.[55][56]

FAOR, MOR and EOR experiments were performed on G-Au@Pt, Figure S17. Significantly lower current densities are recorded in all the fuels. The absence of Cys linkers inhibited electrocatalysis, resulting in 3.6, 16.8 and 9.1 times lower catalytic currents than for G-Cys-Au@Pt during FAOR, MOR and EOR, respectively.

This broadly observed improvement for G-Cys-Au@Pt over C-Pt and G-Au@Pt originates from (1) the large amount of available Pt atoms at the surface shell structures of G-Cys-Au@Pt, (2) the engineered electron pathway and (3) beneficial synergy between Au_{core} and Pt_{shell}. Stronger molecular interactions with Au-modified Pt shells provide extremely active sites for

biofuel oxidation. As-presented catalytic robustness of G-Cys-Au@Pt towards FAOR, MOR and EOR ensures further application within direct formic acid fuel cell (DFAFC), direct methanol fuel cell (DMFC) and direct ethanol fuel cell (DEFC) systems as the anode catalyst.

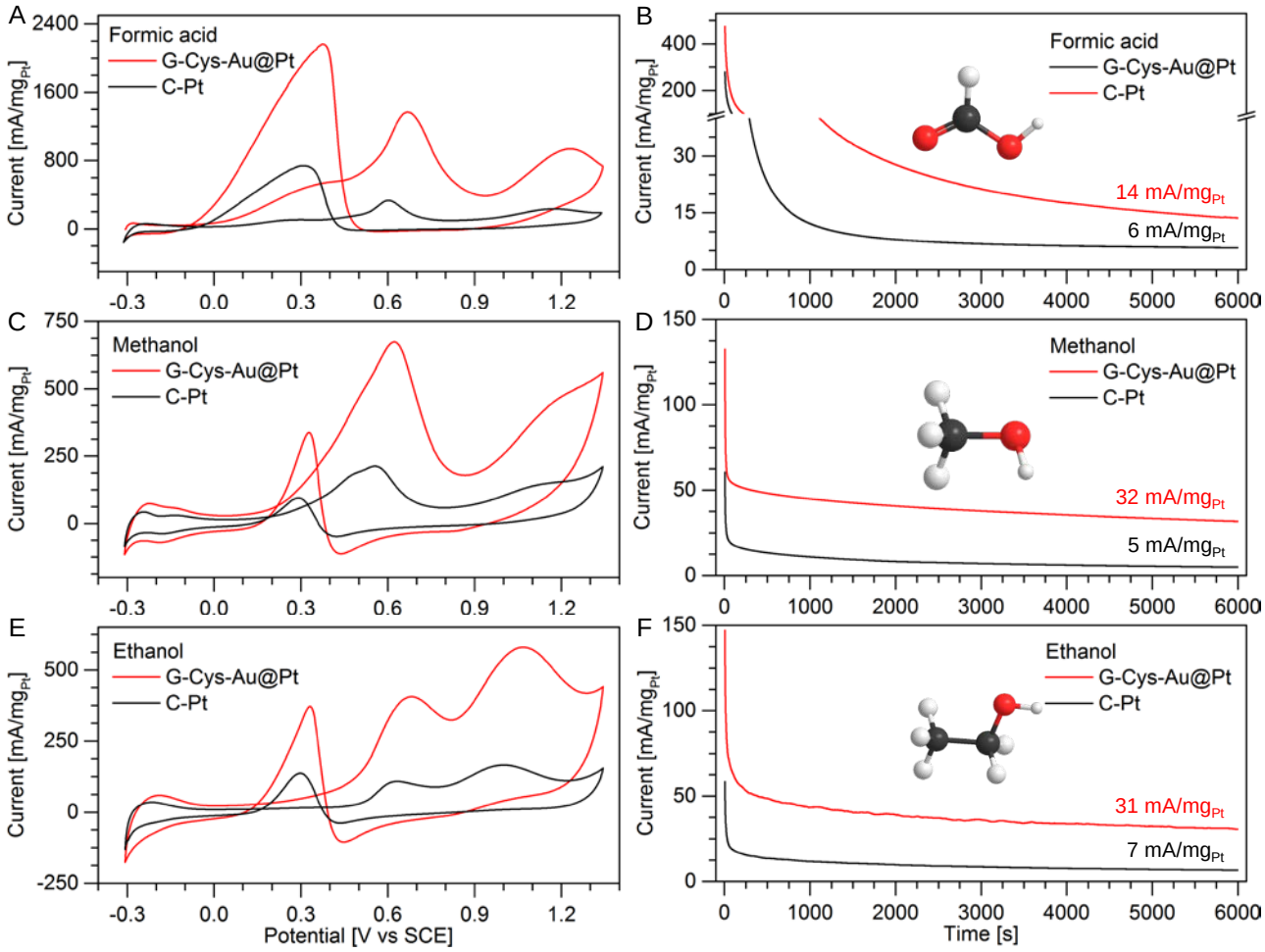

Figure 5. Cyclic voltammograms of G-Cys-Au@Pt (red) and C-Pt (black) during electrochemical oxidation of 0.10 M (A) FA, (C) MeOH and (E) EtOH at 50 mV s^{-1}. Chronoamperometric (CA) response of G-Cys-Au@Pt and C-Pt in 0.10 M (B) FA at 0.10 V, (D) MeOH at 0.3 V, and (F) EtOH at 0.3 V. The supporting electrolyte in all the measurements was 0.10 M H_2SO_4.

2.4 Functional tests in fuel cell systems

FC performance experiments were carried out using an in-house fuel cell stations of DFAFC, DMFC and DEFC systems with membrane electrode assemblies (MEAs) of 1.0 cm^2 active surface, containing C-Pt or G-Cys-Au@Pt catalysts in the anode electrode setup, Figure 6. The cathode was made of commercially available Pt NPs on activated carbon sheets, 1.0 $mg_{Pt}cm^{-2}$. The FC catalytic evaluation was assessed by measuring open circuit voltages (OCVs)and the corresponding power density curves at 40, 60 and 80 °C. The fuels were fed to the anode at a flow rate of 2.0 mL min^{-1} with concentrations of 3.0 and 1.0 M for FA and MeOH/EtOH, respectively, without additional supporting electrolytes to boost the catalytic activity. Dry dioxygen was delivered to the cathode at the flow rate of 100 mL min^{-1}. The G-Cys-Au@Pt catalyst performance in DFAFC, DMFC and DEFC is shown in the Figure 6A-C respectively, and compared to the standard performance of C-Pt, Figure 6D-F and S9. The recorded OCVs and power densities for G-Cys-Au@Pt are given in Table S1. As an example, OCVs and power densities at 80 °C on G-Cys-Au@Pt FCs are 0.830 V and 127 mW cm^{-2} for DFAFC, 0.510 V

and 41 mW cm^{-2} for DMFC, 0.490 V and 9.3 mW cm^{-2} for DEFC. These measurements represent an increase of 153, 52 and 35 mV in OCV, and 95.4, 53.4 and 106.7 % in power density in the DFAFC, DMFC and DEFC setups, respectively, for G-Cys-Au@Pt compared to the C-Pt catalyst (Figure S19). It is clear, that the superior performance observed in electrocatalytic oxidation experiments was preserved in the fuel cell systems.

Electrocatalytic performance of G-Cys-Au@Pt was also tested as the cathode catalyst in the FCs. However, there was no improvement for the FC systems (Figure S20). It is obvious that the diffusion properties of the graphene support within the catalyst layers play a key role and effectively diminish the reactant concentration at the catalytic sites of G-Cys-Au@Pt. Recent studies by Kim et al. [57] and Ma et al. [58] reported a similar observation. By the selective wetting of the ordinarily hydrophobic graphene surface, water molecules are able to interact with the graphene support, space out the sheets and diffuse into the graphene framework at unusually fast rates. The dry gas flow to the heated FC cathode catalyst leads to a compact structure of the graphene layer inhibiting sufficient dioxygen flux to reactive sites on the Pt shell. Humidification of the oxygen flow prior to contacting the FC cathode catalyst layer could potentially lead to an excellent performance of G-Cys-Au@Pt as the ORR catalyst.

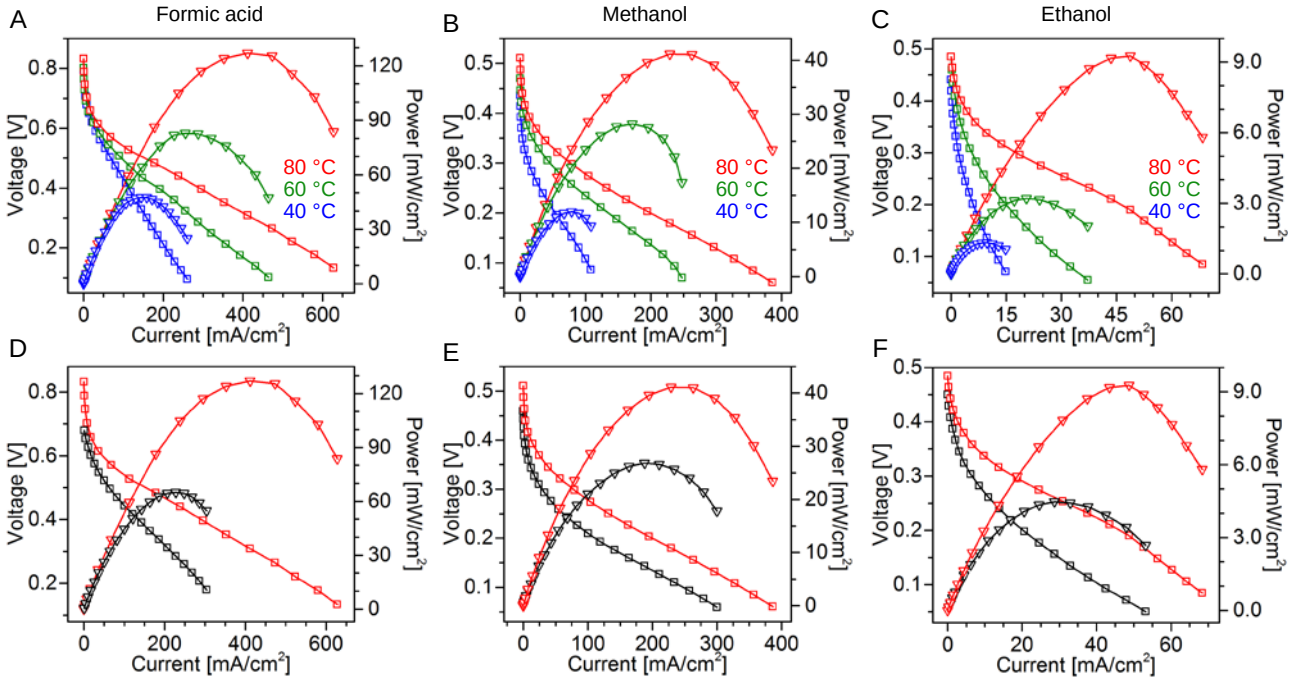

Figure 6. FC performance for G-Cys-Au@Pt catalyst in (A) 3.0 M FA, (B) 1.0 M MeOH and (C) 1.0 M EtOH at 40 (blue), 60 (green) and 80 ºC (red). Comparison of FC performance at 80 ºC for G-Cys-Au@Pt (red) and C-Pt (black) in (D) 3.0 M FA, (E) 1.0 M MeOH and (F) 1.0 M EtOH. G-Cys-Au@Pt loadings were 0.64 mg_{Pt} cm^{-2} (FA), 0.52 mg_{Pt} cm^{-2} (MeOH) and 0.50 mg_{Pt} cm^{-2} (EtOH). C-Pt anode loadings were 0.52 mg_{Pt} cm^{-2} (FA), 0.52 mg_{Pt} cm^{-2} (MeOH) and 0.50 mg_{Pt} cm^{-2} (EtOH). Commercial 1.0 mg_{Pt} cm^{-2} catalyst was used as cathode in all assembled MEAs. Fuel flow was 2.0 mL min^{-1}, non-humidified O_2 flow 100 mL min^{-1}. In all the figures (□) represents voltage and (▽) power plots.

G-Au@Pt was tested in DFAFC and DMFC as anode catalyst, Figure S21. The highest recorded OCVs and power densities for G-Au@Pt are: 0.812 V and 13.1 mW cm^{-2} for DFAFC, and 0.539 V and 3.6 mW cm^{-2} for DMFC. Although the Pt loading of G-Au@Pt was 1.0 mg_{Pt} cm^{-2}, 9.7 and 11.4 times lower power densities than for G-Cys-Au@Pt were recorded at 80 °C in DFAFC and DMFC, respectively. The electron transfer is greatly hampered in G-Au@Pt due to the

absence of a well-defined electron pathway between Au@Pt NPs and graphene. Covalently interconnected G-Cys-Au@Pt outperforms G-Au@Pt by an order of magnitude.

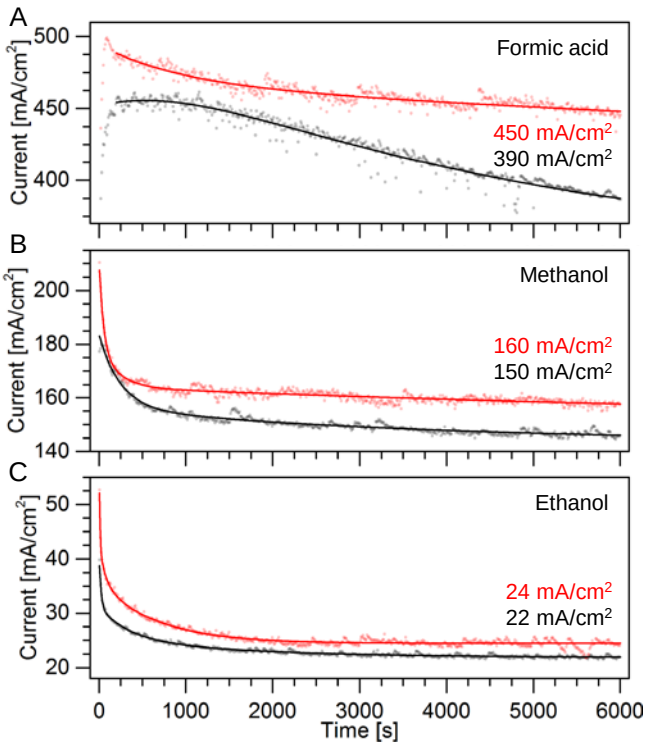

Figure 7. CA plots displaying catalyst stability in FCs at 80 ºC for G-Cys-Au@Pt (red) and C-Pt (black) fed by (A) 3.0 M FA, (B) 1.0 M MeOH and (C) 1.0 M EtOH. CA was performed at the potential corresponding to the maximum power output for 6000 s.

To investigate the stability of the G-Cys-Au@Pt catalyst in the DFAFC, DMFC and DEFC systems, chronoamperometry measurements were performed. The E_{ox} was maintained at the peak power of both catalysts for 6000 s. The current density vs. time plots are shown in Figure 7. The G-Cys-Au@Pt catalyst exhibits higher currents than C-Pt for all the FC setups over the duration of the measurements demonstrating its superior performance. G-Cys-Au@Pt retains 16, 7 and 9 % higher currents than C-Pt, in DFAFC, DMFC and DEFC setups, respectively and generally shows significantly slower deactivation. This is most pronounced for FAOR. The current density degradation observed for both catalysts occurs from the gradual accumulation of CO_{ads}. The current stabilization observed for G-Cys-Au@Pt is attributed to the improved poisoning tolerance and more facile CO_{ads} removal.

3. Conclusions

We have studied several anodic and cathodic fuel cell related electrochemical processes both directly in aqueous media and in fuel cells using G-Cys-Au@Pt NPs with atomically thin Pt shells as electrocatalysts. The particles were prepared by a green and facile chemical synthesis route. The monodisperse 9.5 ± 2 nm Au@Pt NPs with atomically-thin Pt shells were prepared by a green and facile route, and covalently immobilized via the amino acid L-cysteine on a graphene support to generate the G-Cys-Au@Pt nanocatalysts for a range of core fuel cell related processes. The covalent linking provides both rigid covalent NP binding and a facile electron transfer path between the graphene substrate and the NP through the short covalent L-Cys linker. It was ascertained that the G-Cys-Au@Pt remains intact throughout all voltammetric cycles, with no sign of oxidation of the L-Cys linker. This is likely to be caused

at least in part by negative electrostatic NP charging resulting from charge transfer from the thiol group of L-Cys and binding of L-Cys as a –S• radical.
Together with synergy of the Au cores and the Pt shell this new G-Cys-Au@Pt system gave significantly enhanced electrocatalysis of the oxidation of a number of core fuel molecules compared both with G-Au@Pt without L-Cys linker and with the commercial C-Pt catalysts. G-Au@Pt thus showed an order of magnitude lower electrocatalytic performance for fuel oxidation in aqueous media and in FCs, as well as a large overpotential towards the ORR. As an anode catalyst G-Cys-Au@Pt exhibited 4.4, 3.2 and 3.8 higher FAO, MOR and EOR currents than the commercial C-Pt catalyst. As a cathode catalyst, G-Cys-Au@Pt gave an activity increase of 43 A g_{Pt}^{-1} (at 0.900 V vs. RHE) and 25 mV overpotential reduction for the ORR. The G-Cys-Au@Pt catalysts were tested in DFAFC, DMFC and DEFC systems and exhibited maximum power outputs of 127.0, 41.1 and 9.3 mW cm^{-2}, respectively at 80 ºC. Moreover, the catalyst stability was studied by chronoamperometry, and the retained current densities at the conclusion of the chronoamperograms found to be 16, 7 and 9 % greater for G-Cys-Au@Pt than for C-Pt in DFAFC, DMFC and DEFC. This is due to ~14 % increase in CO_{ads} poisoning tolerance and 68 mV lower CO desorption potential.
The high performance and catalytically robust of G-Cys-Au@Pt towards the fuel oxidation and ORR compared to G-Au@Pt and commercial C-Pt offers a perspective for real DFAFC, DMFC and DEFC system applications based on this new catalyst system. In conclusion, G-Cys-Au@Pt is a Pt-efficient, new type of carefully tailored catalyst that offers both high performance and long-term durability.

4. Experimental Section

4.1. Chemicals

Graphite powder (< 20 μm particles), 1-Ethyl-3-(3-dimethylaminopropyl)carbodiimide ($C_8H_{17}N_3$·HCl, EDC, ≥ 98.0 %) and N-Hydroxysuccinimide ($C_4H_5NO_3$, NHS, 97.0 %), 2-(N-morpholino) ethanesulfonic acid ($C_6H_{13}NO_4S$·xH_2O, MES, ≥ 99.5 %), gold (III) chloride trihydrate, ($HAuCl_4$·3H_2O, ≥ 99.9 %), chloroplatinic acid hydrate (H_2PtCl_6·xH_2O, ≥ 99.9%), D-(+)-glucose ($C_6H_{12}O_6$, ≥ 99 %), nitric acid (HNO_3, ≥ 65 %), potassium hydroxide (KOH, 99.99 %), Nafion® ($C_7HF_{13}O_5S$·C_2F_4·xH_2O, 5 wt.%), Pt on graphitized carbon (< 5 nm NPs, 20 wt. %), formic acid (HCOOH, 98.0 – 100 %) and methanol (CH_3OH, ≥ 99.9 %) were all from Sigma-Aldrich. L-cysteine ($C_3H_7NO_2S$, ≥ 99.5 %) and sulfuric acid (H_2SO_4, ≥ 95 %, TraceSELECT® Ultra) were from Fluka, and ethanol (C_2H_6O, ≥ 99.9 %) from Uvasol. 0.10 M MES buffer was adjusted by KOH to pH = 7.0. All chemicals were used as received. All solutions were prepared with ultrapure water (18.2 MΩ·cm).

4.2. Syntheses of G-Cys-Au@Pt

Chemical syntheses of the graphene nanocatalyst includes three main steps, Figure S2. Each step is described here.

4.2.1 Synthesis of G-Cys

98.5 mg of EDC dissolved in 0.5 mL water was slowly added to 98.0 mL, 0.208 mg mL^{-1} GO solution and stirred at room temperature for 10 min followed by sonication for 45 min. 59.8 mg of NHS dissolved in 0.5 mL water was added to the solution and stirred for 10 min followed by sonication at room temperature for 45 min. 63.0 mg of Cys dissolved in 1.0 mL water was added to the solution and heated at 80 °C for 8 hours in a round-bottomed flask, with a condenser

setup. During the reaction, the solution changed color from brown to black. This was followed by sonication for 1 hour and purification by a minimum 3 centrifugation cycles to remove excess chemicals and impurities. Each centrifugation cycle was performed at 12k rpm for 10 min, discarding the supernatant and re-dispersing the residue. Purified G-Cys was finally re-dispersed in 50 mL water resulting in concentrations of 0.40 mg mL^{-1}.

4.2.2 Synthesis of G-Cys-Au@Pt

A solution containing 2.5 mL 0.10 M MES (pH = 7.03), 2.5 mL 0.10 M glucose, 8.75 mL 0.40 mg mL^{-1} G-Cys and 8.75 mL ultrapure water was heated at 95 °C for 10 minutes in a water bath, followed by addition of 2.5 mL of 20.3 mM $HAuCl_4$ for 1 hour at 95 °C for Au NP formation. G-Cys-Au solution had a dark red color. After the Au NP seed formation, 74.0 mL of water was added to the flask followed by 1.0 mL of 20.0 mM H_2PtCl_6 and continued heating at 70 °C for 2 hours to obtain an atomically thin Pt layer on Au NP seeds. The final G-Cys-Au@Pt solution was dark brown. The solution was then sonicated for 1 hour and purified by 4 centrifugation cycles. Purified G-Cys-Au@Pt was kept in a highly condensed state to be drop-casted on electrodes or carbon paper for MEAs.

4.3. Electrode polishing and cleaning

All glassware was cleaned by boiling in 15 % HNO_3 solution followed by washing in ultrapure water. The glassy carbon electrode (GCE, ϕ = 4.0 mm, A = 0.1256 cm^2) and rotating ring (Pt) disk (GCE) electrode (RRDE, ϕ_{disk} = 5.61 mm, A_{disk} = 0.2472 cm^2, $\phi_{ring\ (inner)}$ = 6.25 mm, $\phi_{ring\ (outer)}$ = 7.92 mm, A_{ring} = 0.1859 cm^2, ring collection efficiency = 37 %) was first wet-polished by sand paper (grit roughness 2000, followed by 4000) for 10 min by hand. They were further polished by Al_2O_3 slurry (particle diameter sizes of 1.0, 0.3 and 0.05 µm), using the largest particle size first (rough polishing) and finishing with the finest particle size (mirror-like electrode surface finish). The electrodes were sonicated in ultrapure water for 30 min in total with intermittent water exchange (1. time after 5 min, 2. time after 10 min and 3. time after 15 min). Freshly cleaned electrodes were dried in the fume hood at room temperature for 5 min. prior to drop-casting. The RRDE was purchased from Pine Research Instrumentation, Inc. (USA).

4.4. Drop-casting of catalysts for electrochemical experiments

Electrochemical performance of the G-Cys-Au@Pt catalyst was compared to commercial catalysts from Sigma-Aldrich, 20 wt. % of Pt (NP size ~ 5 nm) on graphitized carbon (C-Pt). The bimetallic structure of G-Cys-Au@Pt contains Au (core) which is not catalytically active towards oxidation of used biofuels or ORR, but Pt (shell material) is a well-known catalyst material for these reactions. Therefore, Pt was maintained in the same amount of catalytic material for all the electrodes. In case of ORR experiments the Pt loading on RRDE was 5 µg (20.2 $\mu g_{Pt}\ cm^{-2}$) while the loading for the rest of the experiments was 3 µg of Pt on GCEs (23.9 $\mu g_{Pt}\ cm^{-2}$). Catalyst layers were protected by 5 µL of 0.05 % Nafion® (dissolved in ethanol). Prior to each electrochemical experiment, all the electrodes were subjected to activation procedure which consists of repetitive voltammetric cycling (more than 30 scans) at a scan rate of 100 mV s^{-1} in pure 0.10 M H_2SO_4, and a narrow potential window ranging from -0.30 to 1.00 V, Figure S11.

4.5. Fuel cell experiments

The performance of the developed catalyst was tested in a PEMFC system. The anode electrodes were prepared by catalyst ink drop-casting on microporous carbon paper Toray (Japan), reaching the loading from 0.50 to 0.68 mgPt cm^{-2}. The cathode used was a commercial catalyst electrode BC-H225-10F (Quintech, Germany) with loading of 1.0 mgPt cm^{-2}. The membrane electrode assembly (MEA) was prepared by hot-pressing the two electrodes and Nafion™-115 membrane (Quintech, Germany) at 135.0 °C and a pressure of 120.0 kg cm^{-2}. The MEA active area was 1.0 cm^2. An in-house FC test station based on PEMFC, equipped with heating thermocouples type K, flow of fuel molecules and O_2 was controlled by an in-house procedure in the LabVIEW 2015 software. The FC test station was built up according to standards of practice.[16][59] The FC was operated at 40, 60 and 80 °C. The fuel flow was kept constant at 2.0 mL min^{-1}. The O_2 flow rate was 100 mL min^{-1} without humidification process.

4.6. Characterization techniques

TEM analyses of the samples were carried out using a Tecnai G20 instrument operating at 200 kV and equipped with an X-ray spectrometer (EDX) from FEI Company (Oregon, USA). X-ray photoelectron spectroscopy (XPS) was carried out using an ESCALABMKII X-ray photoelectron spectrometer (Thermo Scientific™, USA). UV–vis spectra were recorded using a single-beam spectrophotometer (HP8453, Hewlett Packard, USA).
All electrochemical measurements were performed at room temperature (20 ± 2° C) using an Autolab System (Eco Chemie, Netherlands) controlled by the GPES/NOVA 1.11 software inside a Faradaic cage. The RRDE experiments were performed within the fume hood instead the Faradaic cage. Unless stated otherwise, all the measurements were performed in 0.10 M H_2SO_4 under acidic condition (pH ≈ 1.0) with a three-electrode system consisting of the glassy carbon electrode (GCE) as working electrode (WE), a reversible hydrogen electrode (RHE) as reference electrode (RE), and a platinum coiled wire with a large surface area as counter electrode (CE). The CE was cleaned in a hydrogen flame followed by washing at least 3 times with ultrapure water. A fresh RHE was prepared prior to each of the experiments using the same supporting electrolyte as for the measurements. After the measurements, the RHE potential was measured against a saturated calomel electrode (SCE) and all results are reported against the SCE. All glassware including electrochemical cells was boiled in 15 % HNO_3 for 20 minutes, copiously washed with ultrapure water and sonicated for 30 minutes in two intervals, prior to each of the experiments.

Acknowledgements

Financial support from the Danish Council for Independent Research (DFF – 1335-00330) to JZ, the Danish Council for Independent Research (DFF 5054-00107) to CE, and Innovation Fund Denmark (12-132710) to HAH is acknowledged. We appreciate the assistance of Lars Nilausen Cleemann and Larissa Seerup at Department of Energy Conversion and Storage, DTU for the help in fuel cell station assembly and TGA measurements.

Received: ((will be filled in by the editorial staff))
Revised: ((will be filled in by the editorial staff))
Published online: ((will be filled in by the editorial staff))

References

[1] A. Brouzgou, S. Q. Song, P. Tsiakaras, *Appl. Catal. B Environ.* **2012**, *127*, 371.

[2] H. Tang, Y. Zeng, D. Liu, D. Qu, J. Luo, K. Binnemans, D. E. De Vos, J. Fransaer, D. Qu, S.-G. Sun, *Nano Energy* **2016**, *26*, 131.

[3] C. Zhao, P. Gai, R. Song, Y. Chen, J. Zhang, J.-J. Zhu, *Chem. Soc. Rev.* **2017**, *46*, 1545.

[4] M. Shao, A. Peles, K. Shoemaker, *Nano Lett.* **2011**, *11*, 3714.

[5] N. M. Marković, P. N. Ross, *Surf. Sci. Rep.* **2002**, *45*, 117.

[6] J. Zhang, K. Sasaki, E. Sutter, R. R. Adzic, *Science* **2007**, *315*, 220.

[7] M. C. Daniel, D. Astruc, *Chem. Rev.* **2004**, *104*, 293.

[8] Z. X. Liang, T. S. Zhao, J. B. Xu, *J. Power Sources* **2008**, *185*, 166.

[9] C. Engelbrekt, N. Šešelj, R. Poreddy, A. Riisager, J. Ulstrup, J. Zhang, *J. Mater. Chem. A* **2016**, *4*, 3278.

[10] M. Min, C. Kim, H. Lee, *J. Mol. Catal. A Chem.* **2010**, *333*, 6.

[11] E. Antolini, *Energy Environ. Sci.* **2009**, *2*, 915.

[12] S. Sharma, B. G. Pollet, *J. Power Sources* **2012**, *208*, 96.

[13] N. Seselj, C. Engelbrekt, J. Zhang, *Sci. Bull.* **2015**, *60*, 864.

[14] L. Xin, F. Yang, S. Rasouli, Y. Qiu, Z. F. Li, A. Uzunoglu, C. J. Sun, Y. Liu, P. Ferreira, W. Li, Y. Ren, L. A. Stanciu, J. Xie, *ACS Catal.* **2016**, *6*, 2642.

[15] B. P. Vinayan, S. Ramaprabhu, *Nanoscale* **2013**, *5*, 5109.

[16] C. Venkateswara Rao, C. R. Cabrera, Y. Ishikawa, *J. Phys. Chem. C* **2011**, *115*, 21963.

[17] T. Palaniselvam, V. Kashyap, S. N. Bhange, J. B. Baek, S. Kurungot, *Adv. Funct. Mater.* **2016**, 2150.

[18] A. Halder, M. Zhang, Q. Chi, *Biosens. Bioelectron.* **2017**, *87*, 764.

[19] S. G. Jang, A. Khan, M. D. Dimitriou, B. J. Kim, N. A. Lynd, E. J. Kramer, C. J. Hawker, *Soft Matter* **2011**, *7*, 6255.

[20] J. Shang, L. Ma, J. Li, W. Ai, T. Yu, G. G. Gurzadyan, *Sci. Rep.* **2012**, *2*, 792.

[21] R. K. Biroju, B. Choudhury, P. K. Giri, *Catal. Sci. Technol.* **2016**, *6*, 7101.

[22] Q. Chi, J. Zhang, J. E. T. Andersen, J. Ulstrup, *J. Phys. Chem. B* **2001**, *105*, 4669.

[23] W. Liu, D. Sun, J. Fu, R. Yuan, Z. Li, *RSC Adv.* **2014**, *4*, 11003.

[24] R. Brito, V. A. Rodríguez, J. Figueroa, C. R. Cabrera, *J. Electroanal. Chem.* **2002**, *520*, 47.

[25] J. Huang, J. C. Hemminger, *J. Am. Chem. Soc.* **1993**, *115*, 3342.

[26] D. Y. Petrovykh, H. Kimura-Suda, A. Opdahl, L. J. Richter, M. J. Tarlov, L. J. Whitman, *Langmuir* **2006**, *22*, 2578.

[27] J. W. Lee, W. Jung, *J. Ind. Eng. Chem.* **2014**, *20*, 2883.

[28] C. Zhang, L. Fu, N. Liu, M. Liu, Y. Wang, Z. Liu, *Adv. Mater.* **2011**, *23*, 1020.

[29] G. M. Veith, A. R. Lupini, L. Baggetto, J. F. Browning, J. K. Keum, A. Villa, L. Prati, A. B. Papandrew, G. A. Goenaga, D. R. Mullins, S. E. Bullock, N. J. Dudney, *Chem. Mater.* **2013**, *25*, 4936.

[30] P.-P. Zuo, H.-F. Feng, Z.-Z. Xu, L.-F. Zhang, Y.-L. Zhang, W. Xia, W.-Q. Zhang, *Chem. Cent. J.* **2013**, *7*, 39.

[31] N. Spãtaru, B. V Sarada, E. Popa, D. A. Tryk, A. Fujishima, *Anal. Chem.* **2001**, *73*, 514.

[32] N. Ossendorfová, J. Pradáč, J. Koryta, *J. Electroanal. Chem. Interfacial Electrochem.* **1970**, *28*, 311.

[33] V. A. Bogdanovskaya, A. Y. Safronov, M. R. Tarasevich, A. S. Chernyak, *J. Electroanal. Chem. Interfacial Electrochem.* **1986**, *202*, 147.

[34] T. R. Ralph, M. L. Hitchman, J. P. Millington, F. C. Walsh, *J. Electroanal. Chem.* **1994**, *375*, 1.

[35] A. Lerf, H. He, M. Forster, J. Klinowski, *J. Phys. Chem. B* **1998**, *102*, 4477.

[36] D. R. Dreyer, S. Park, C. W. Bielawski, R. S. Ruoff, *Chem. Soc. Rev.* **2010**, *39*, 228.

[37] A. Bakandritsos, M. Pykal, P. Błoński, P. Jakubec, D. D. Chronopoulos, K. Poláková, V. Georgakilas, K. Čépe, O. Tomanec, V. Ranc, A. B. Bourlinos, R. Zbořil, M. Otyepka, *ACS Nano* **2017**, *11*, 2982.

[38] B. Hammer, J. K. Nørskov, *Adv. Catal.* **2000**, *45*, 71.

[39] N. Kristian, Y. Yu, P. Gunawan, R. Xu, W. Deng, X. Liu, X. Wang, *Electrochim. Acta* **2009**, *54*, 4916.

[40] M. D. Obradović, J. R. Rogan, B. M. Babić, A. V Tripković, A. R. S. Gautam, V. R. Radmilović, S. L. Gojković, *J. Power Sources* **2012**, *197*, 72.

[41] H. Kita, H. Nakajima, K. Hayashi, *J. Electroanal. Chem. Interfacial Electrochem.* **1985**, *190*, 141.

[42] E. Herrero, Q.-S. Chen, J. Hernandez, S.-G. Sun, J. M. Feliu, *Phys. Chem. Chem. Phys.* **2011**, *13*, 16762.

[43] B. C. Ong, S. K. Kamarudin, M. S. Masdar, U. A. Hasran, *Int. J. Hydrogen Energy* **2016**.

[44] X. Zhou, J. Qiao, L. Yang, J. Zhang, *Adv. Energy Mater.* **2014**, *4*, 1301523.

[45] M. del Cueto, P. Ocón, J. M. L. Poyato, *J. Phys. Chem. C* **2015**, *119*, 2004.

[46] F. J. Vidal-Iglesias, J. Solla-Gullón, V. Montiel, A. Aldaz, *Electrochem. commun.* **2012**, *15*, 42.

[47] H. Meng, N. Larouche, M. Lefèvre, F. Jaouen, B. Stansfield, J.-P. Dodelet, *Electrochim. Acta* **2010**, *55*, 6450.

[48] H. Okamoto, W. Kon, Y. Mukouyama, *J. Phys. Chem. B* **2005**, *109*, 15659.

[49] Y.-C. Bai, W.-D. Zhang, C.-H. Chen, J.-Q. Zhang, *J. Alloys Compd.* **2011**, *509*, 1029.

[50] C. Xu, Q. Hao, H. Duan, *J. Mater. Chem. A* **2014**, *2*, 8875.

[51] Z. Guo, X. Zhang, H. Sun, X. Dai, Y. Yang, X. Li, T. Meng, *Electrochim. Acta* **2014**, *134*, 411.

[52] W. Huang, H. Wang, J. Zhou, J. Wang, P. N. Duchesne, D. Muir, P. Zhang, N. Han, F.

Zhao, M. Zeng, J. Zhong, C. Jin, Y. Li, S.-T. Lee, H. Dai, *Nat. Commun.* **2015**, *6*, 10035.

[53] H.-J. Qiu, X. Shen, J. Q. Wang, A. Hirata, T. Fujita, Y. Wang, M. W. Chen, *ACS Catal.* **2015**, *5*, 3779.

[54] M. A. F. Akhairi, S. K. Kamarudin, *Int. J. Hydrogen Energy* **2016**, *41*, 4214.

[55] A. De, J. Datta, I. Haldar, M. Biswas, *ACS Appl. Mater. Interfaces* **2016**, *8*, 28574.

[56] Y. Wang, A. Tabet-Aoul, M. Mohamedi, *J. Electrochem. Soc.* **2016**, *163*, F1272.

[57] J.-S. Kim, J. S. Choi, M. J. Lee, B. H. Park, D. Bukhvalov, Y.-W. Son, D. Yoon, H. Cheong, J.-N. Yun, Y. Jung, J. Y. Park, M. Salmeron, *Sci. Rep.* **2013**, *3*, 2309.

[58] M. Ma, G. Tocci, A. Michaelides, G. Aeppli, *Nat Mater* **2016**, *15*, 66.

[59] D. Sebastián, V. Baglio, A. S. Aricò, A. Serov, P. Atanassov, *Appl. Catal. B Environ.* **2016**, *182*, 297.

TOC